Supplementary Information

Defect-surface engineering of La-doped ceria for microwave-assisted hydrogen production

A. Domínguez-Saldaña[1], L. Navarrete[1], A.J. Carrillo[1], M. Balaguer[1], J. Santos[1], B. García-Baños[2], P. Plaza-González[2], D. Catalán-Martínez[1], J.M. Catalá-Civera[2,] *, J.M. Serra[1,] *

[1]Instituto de Tecnología Química, (Universitat Politècnica de València-Consejo Superior de Investigaciones Científicas), Valencia, Spain
[2] Instituto ITACA, (Universitat Politècnica de València), Valencia, Spain
* Correspondence to: jmserra@itq.upv.es, jmcatala@dcom.upv.es.

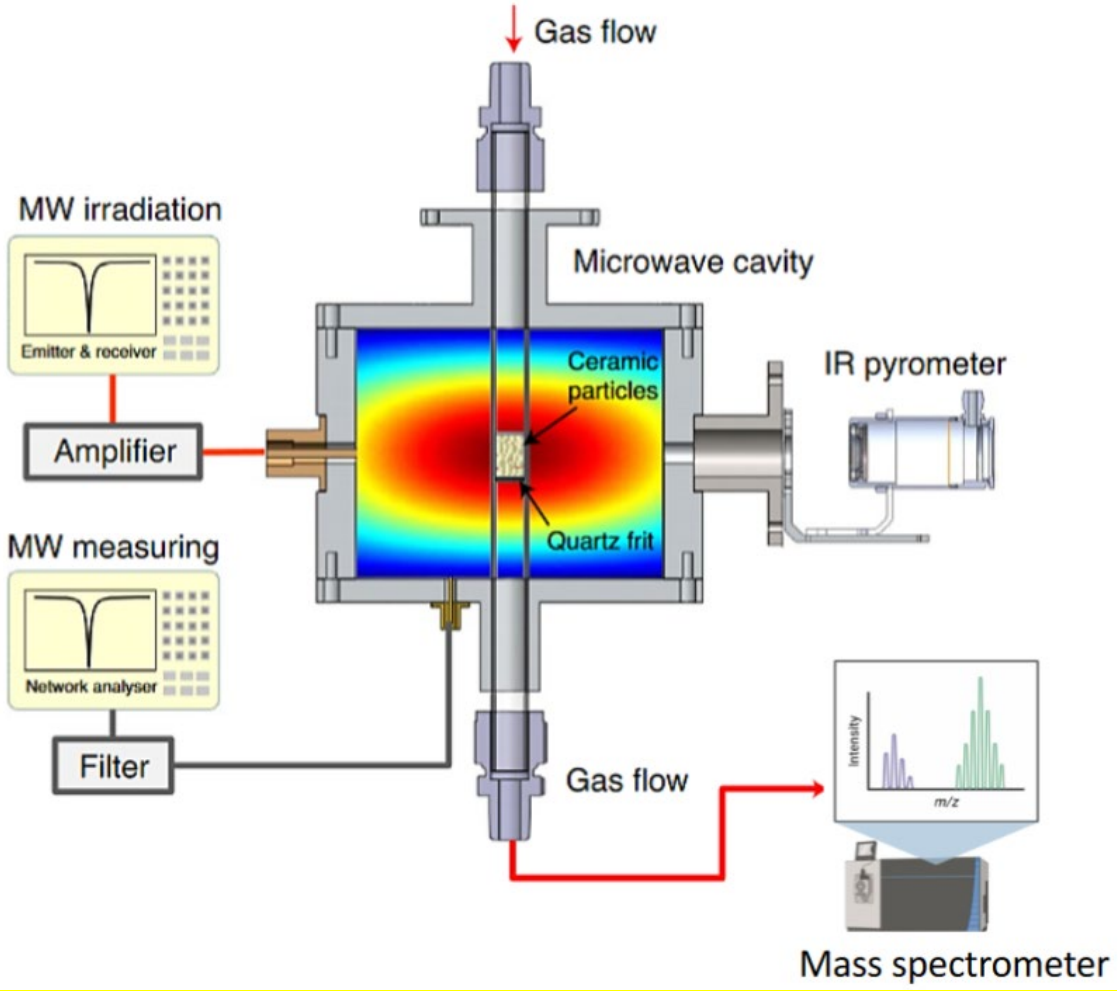

Figure S1: General schematic of the microwave-driven fixed-bed reactor based on a TM_{111} monomode microwave cavity. The electric field is focused on the material, which is placed in the center of the cavity.

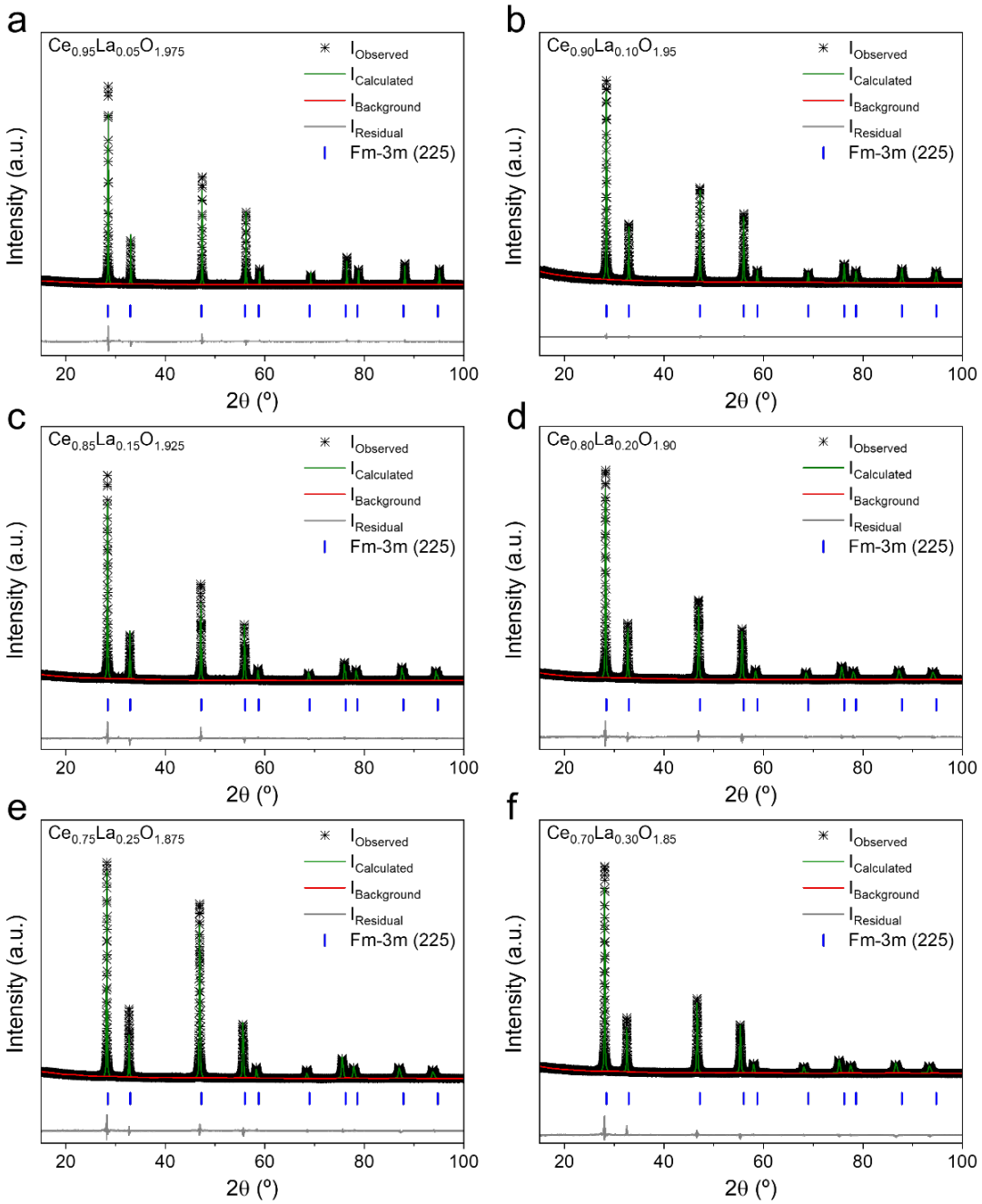

Figure S2. Rietveld refinement for materials based on La-doped ceria ($Ce_{1-x}La_xO_{2-\delta}$; x=0.05 (a), 0.10 (b), 0.15 (c), 0.20 (d), 0.25 (e), 0.30 (f)).

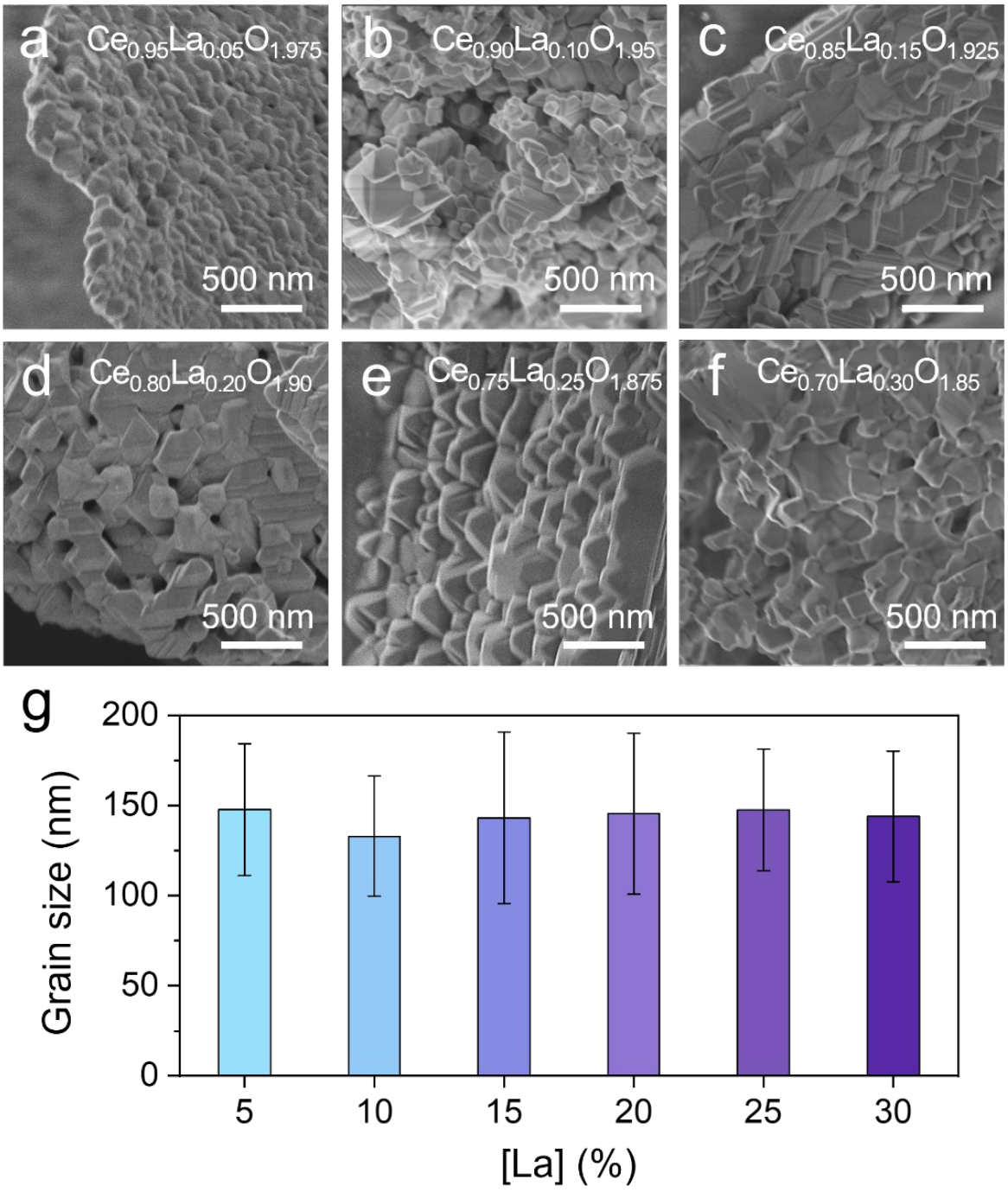

Figure S3. FESEM micrographs for the materials based on La-doped ceria ($Ce_{1-x}La_xO_{2-\delta}$; x=0.05 (a), 0.10 (b), 0.15 (c), 0.20 (d), 0.25 (e), 0.30 (f)), as well as grain size distribution for each of them (g).

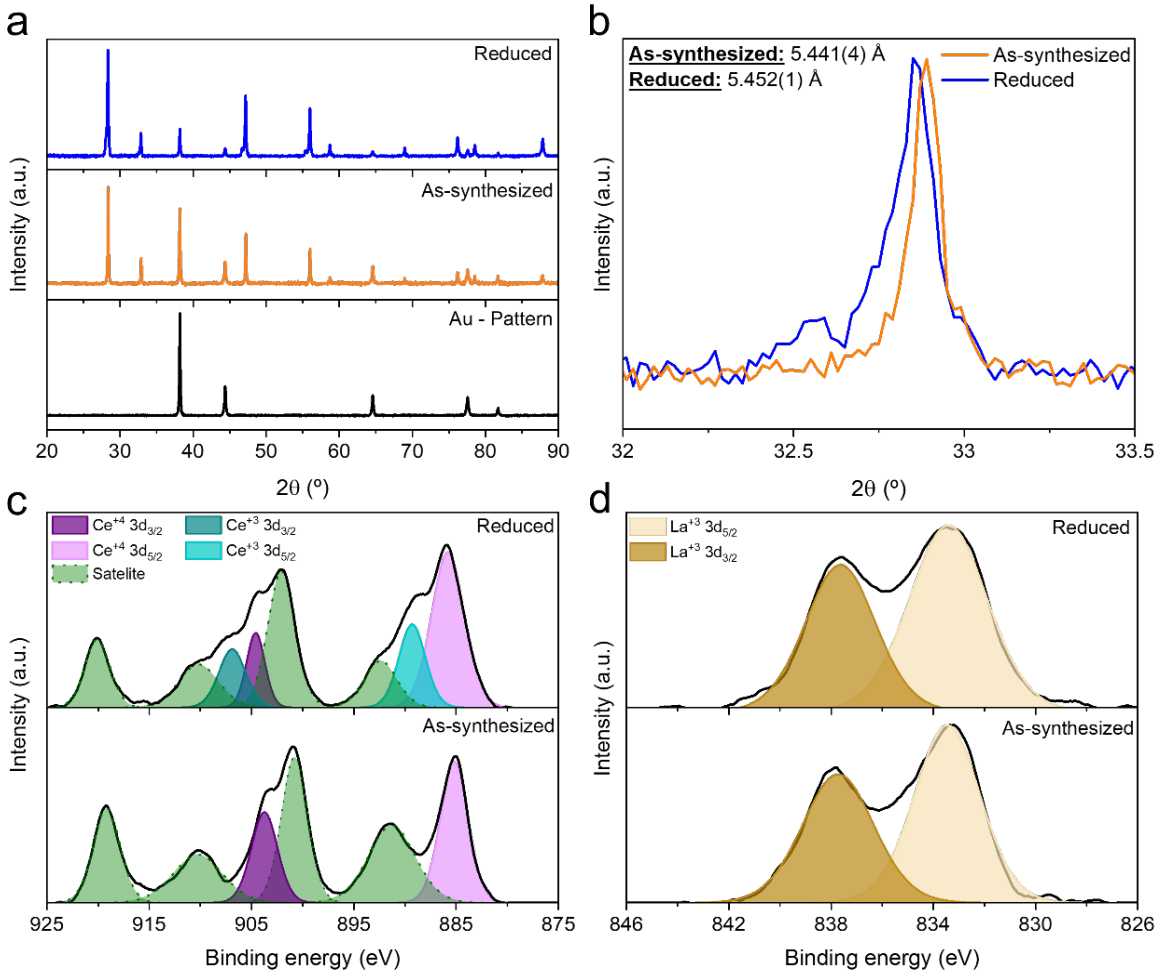

Figure S4. Comparison between the reduced and unreduced materials by XRD and XPS; a) Global diffractograms of the as-synthesized, reduced, and pattern materials; b) Zoom in the region where the highest intensity diffraction maximum is located; c) Region of the XPS spectrum of the 3d orbital of the cerium (c) and lanthanum (d).

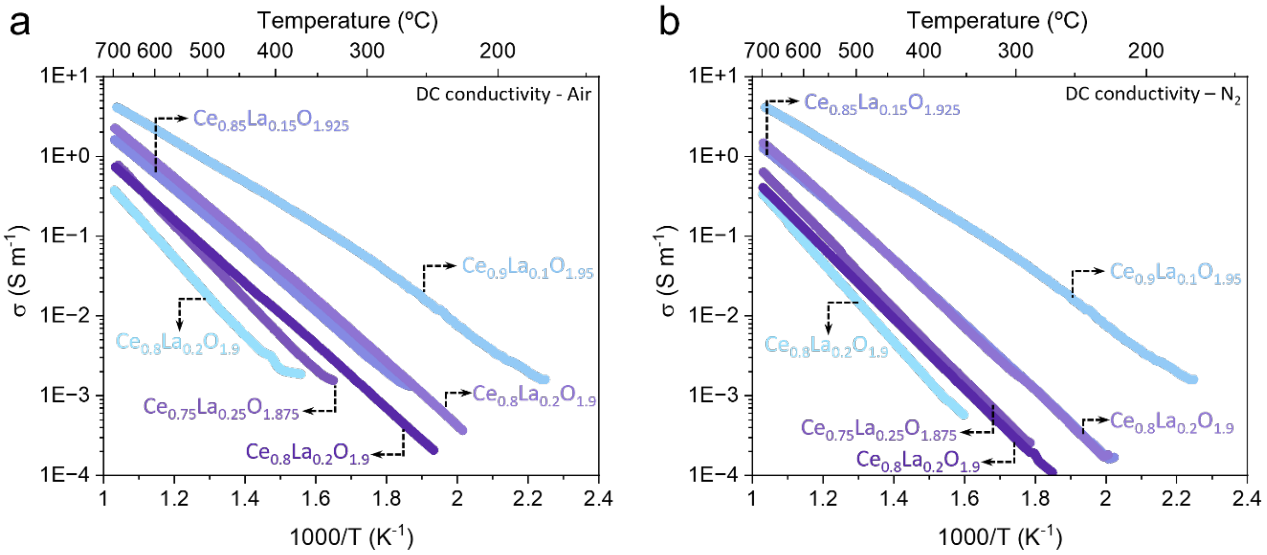

Figure S5. DC conductivity in air (a) and N_2 (b) of oxygen carriers based on La-doped ceria ($Ce_{1-x}La_xO_{2-\delta}$; x=0.05, 0.10, 0.15, 0.20, 0.25, 0.30.)

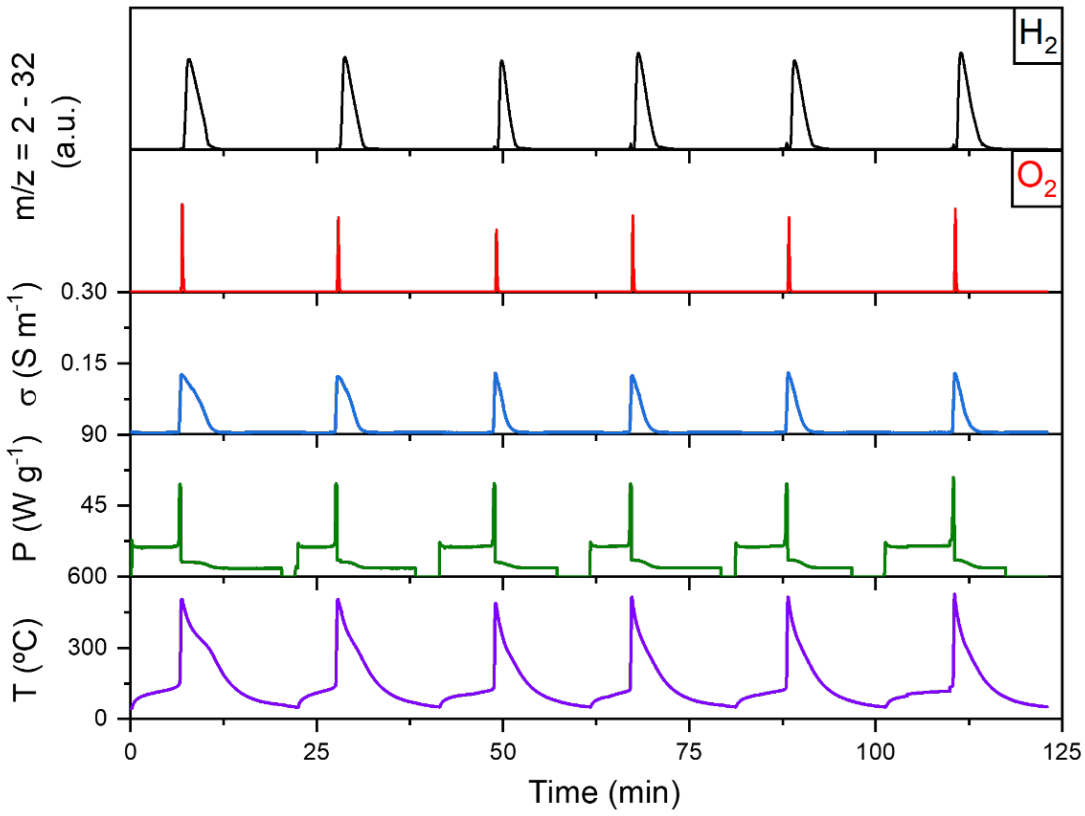

Figure S6. Six cycles of water splitting of the material $Ce_{0.95}La_{0.05}O_{1.975}$, where the signals of O_2 and H_2 in the mass spectrometer are represented in red and black, respectively. As well as the applied power and the in-situ temperature and conductivity of the material, in green, purple, and blue, respectively.

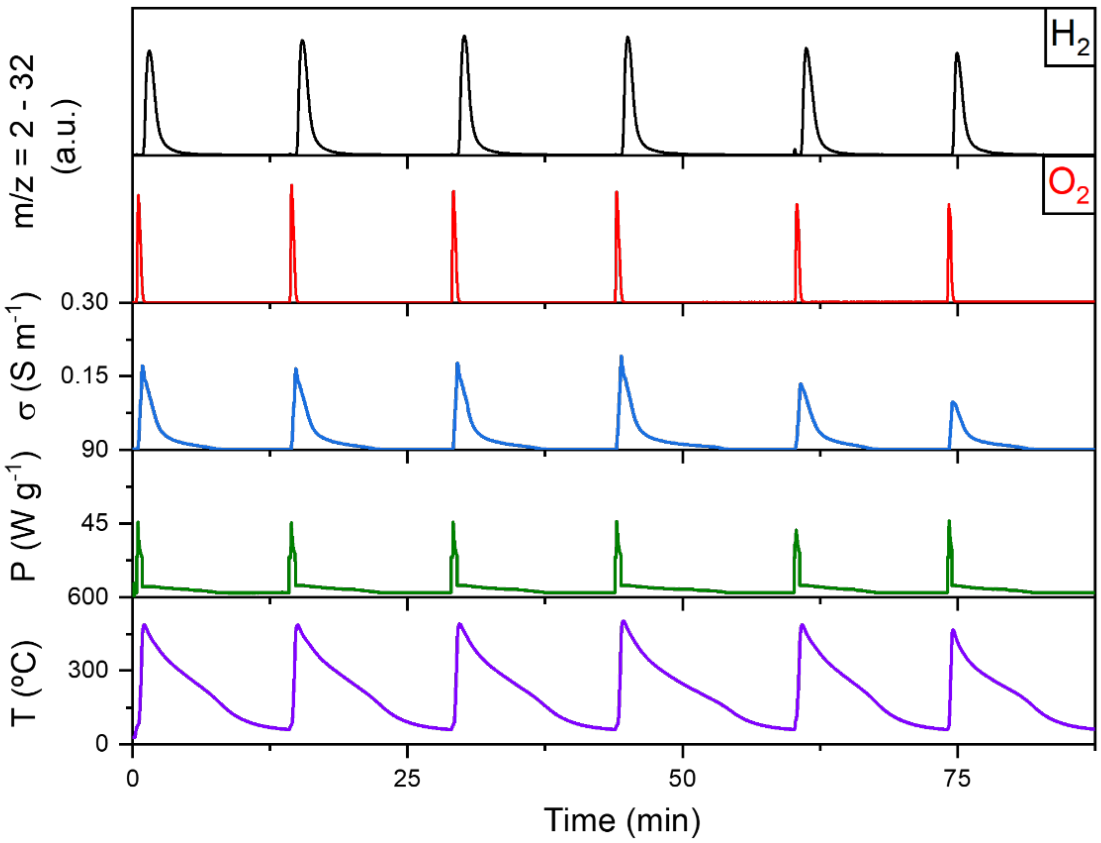

Figure S7. Six cycles of water splitting of the material $Ce_{0.90}La_{0.10}O_{1.95}$, where the signals of O_2 and H_2 in the mass spectrometer are represented in red and black, respectively. As well as the applied power and the in-situ temperature and conductivity of the material, in green, purple, and blue, respectively.

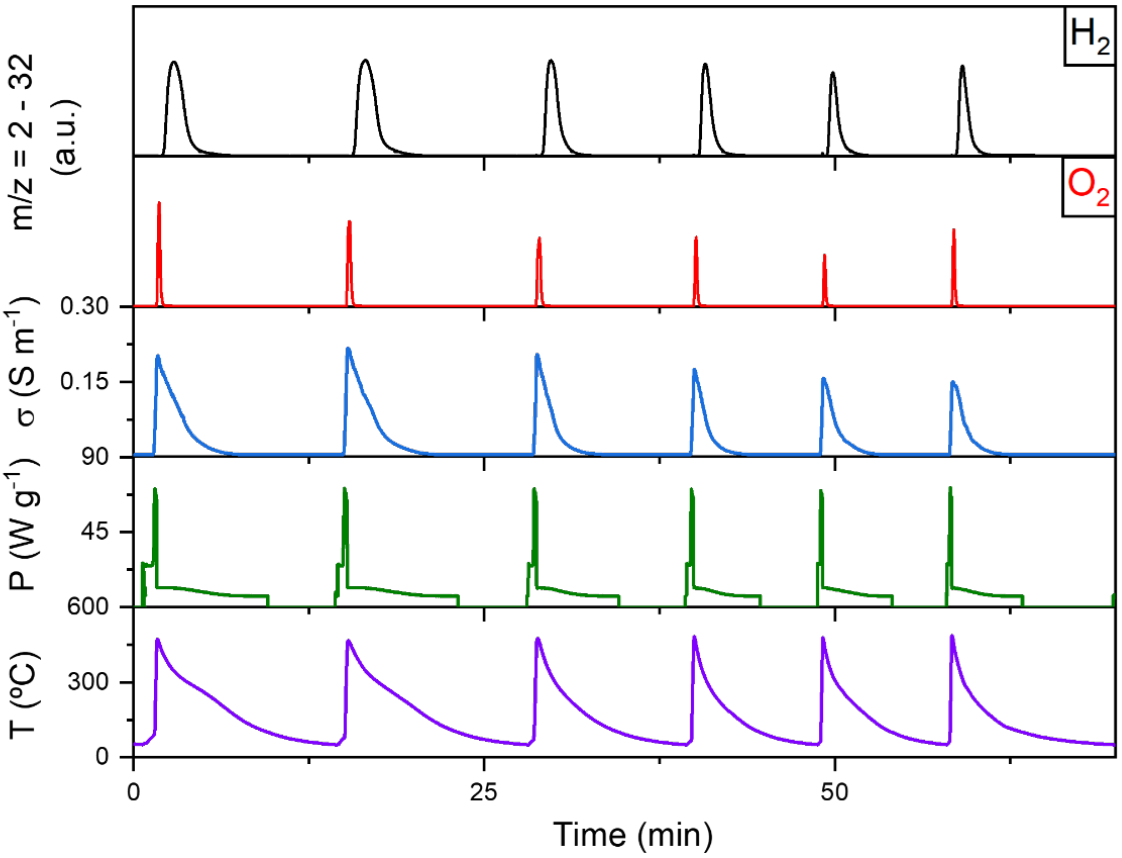

Figure S8. Six cycles of water splitting of the material $Ce_{0.85}La_{0.15}O_{1.925}$, where the signals of O_2 and H_2 in the mass spectrometer are represented in red and black, respectively. As well as the applied power and the in-situ temperature and conductivity of the material, in green, purple, and blue, respectively.

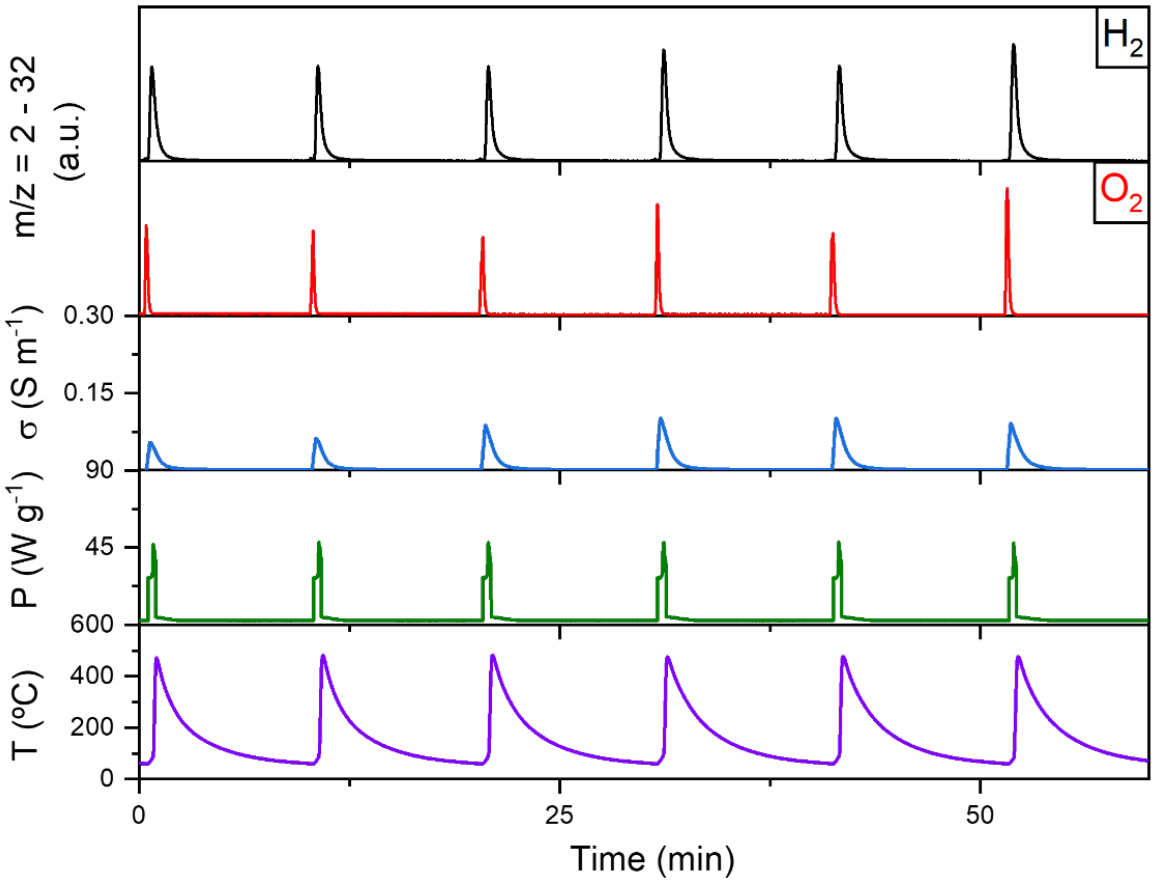

Figure S9. Six cycles of water splitting of the material $Ce_{0.80}La_{0.20}O_{1.90}$, where the signals of O_2 and H_2 in the mass spectrometer are represented in red and black, respectively. As well as the applied power and the in-situ temperature and conductivity of the material, in green, purple, and blue, respectively.

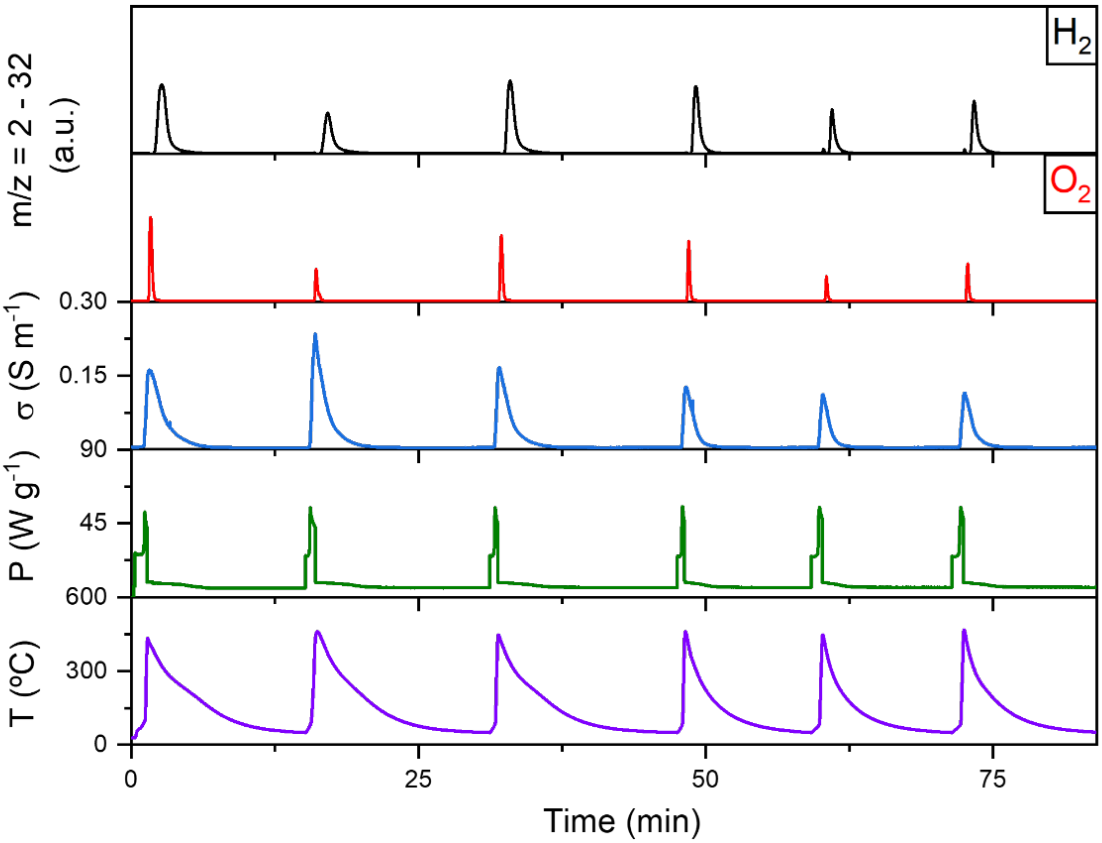

Figure S10. Six cycles of water splitting of the material $Ce_{0.75}La_{0.25}O_{1.875}$, where the signals of O_2 and H_2 in the mass spectrometer are represented in red and black, respectively. As well as the applied power and the in-situ temperature and conductivity of the material, in green, purple, and blue, respectively.

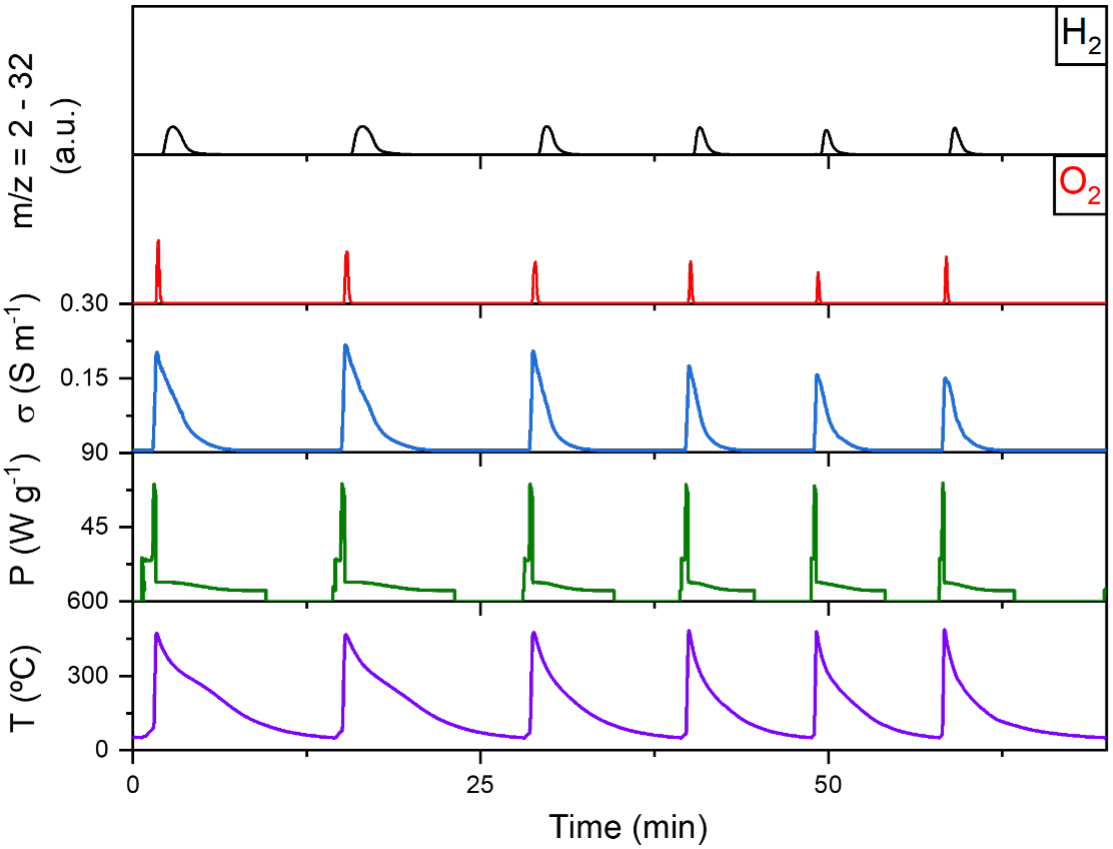

Figure S11. Six cycles of water splitting of the material $Ce_{0.70}La_{0.30}O_{1.85}$, where the signals of O_2 and H_2 in the mass spectrometer are represented in red and black, respectively. As well as the applied power and the in-situ temperature and conductivity of the material, in green, purple, and blue, respectively.

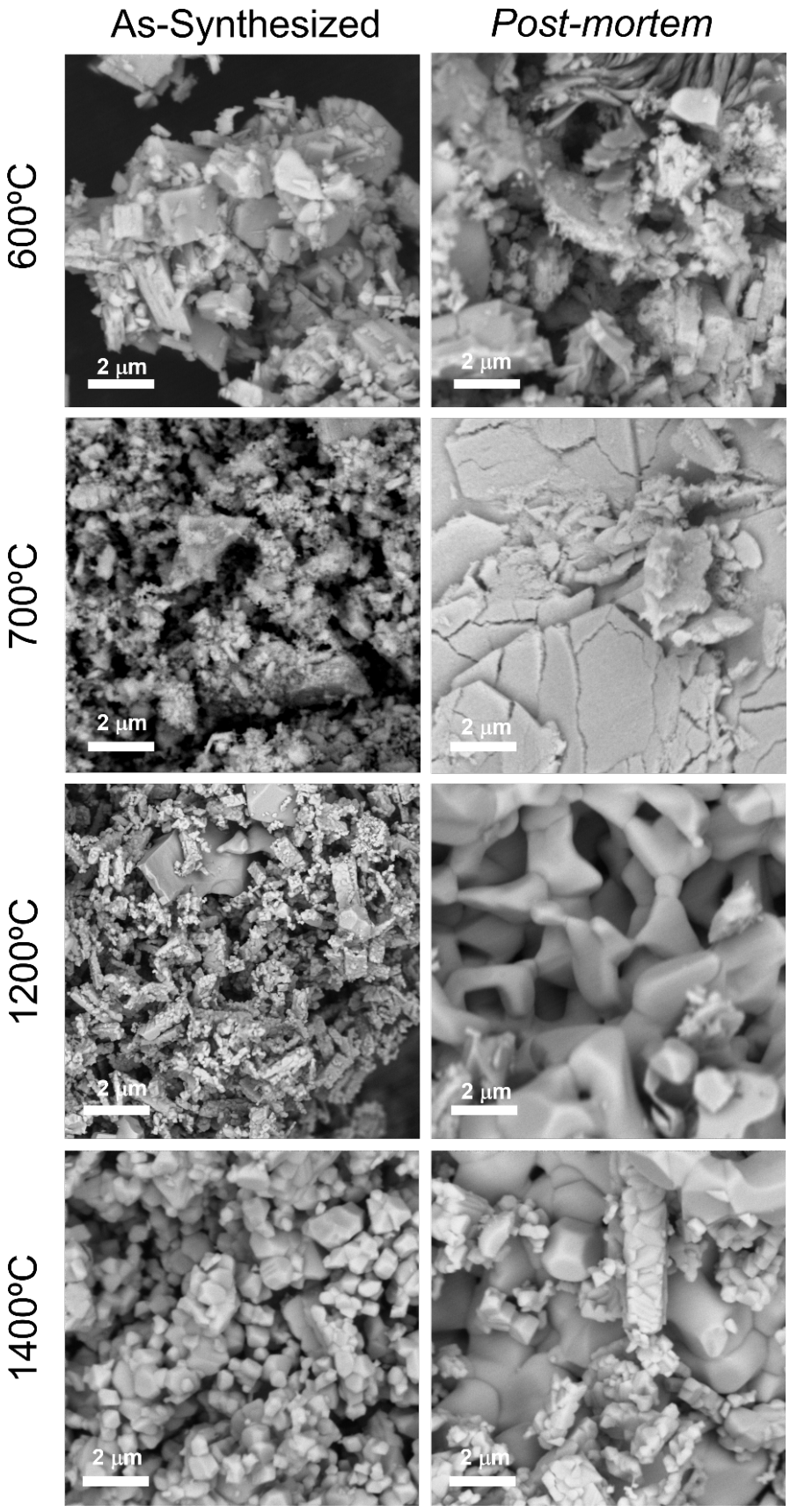

Figure S12. FESEM micrographs of $Ce_{0.9}La_{0.1}O_{2-\delta}$ material, with variable surface area, as-synthesized and post-mortem.